Journal of Materials Chemistry A

RSC Publishing

PAPER

View Article Online
View Journal | View Issue

A high power density electrode with ultralow carbon *via* direct growth of particles on graphene sheets†

Cite this: *J. Mater. Chem. A*, 2013, **1**, 6183

Chek Hai Lim,[a] Aravindaraj G. Kannan,[a] Hyun-Wook Lee[b] and Do Kyung Kim*[a]

The application of lithium ion batteries in high power applications such as hybrid electric vehicles and electric grid systems critically requires drastic improvement in the electronic conductivity using effective materials design and strategies. Here, we demonstrate that the growth of a multi-component structure of composition $LiTi_2(PO_4)_3$ [LTP] on a reduced graphene oxide (rGO) surface *via* a facile synthetic strategy could achieve an ultrahigh rate capability with the total carbon content as low as 1.79 wt%. The rGO–LTP hybrid material has been prepared using a two-step approach, where the growth of TiO_2 nanoparticles on the graphene oxide surface is followed by the high temperature growth of LTP on graphene sheets and simultaneous thermal reduction of graphene oxide. The LTP particles are densely packed within the ripples of rGO and form a compact, well-connected graphene network requiring no additional conductive carbon to facilitate fast electron transport from active materials to the current collector. Here, graphene not only acts as a stable conductive substrate but also helps to control the size of the formed particles. The rGO–LTP hybrid as a cathode in lithium ion batteries achieves an ultrahigh specific power of 10 000 W kg^{-1} at a specific energy of 210 W h kg^{-1}, which corresponds to a charge and discharge time of 36 s and also retains 92% of the initial capacity after 100 cycles at a 10 C charge–discharge rate. Such an excellent performance is attributed to the multifunctional roles performed by rGO such as controlling the particle size, enhancing the electronic conductivity through a highly conductive network and rendering stability during cycling. This provides an effective design strategy for growing complex hybrid materials on graphene and engineering graphene nanosheets for advanced energy storage applications.

Received 17th January 2013
Accepted 23rd March 2013

DOI: 10.1039/c3ta10254h

www.rsc.org/MaterialsA

1 Introduction

Rechargeable lithium ion batteries (LIBs), which are promising systems for storage of electrical energy from intermittent renewable energy sources such as solar and wind to power electric vehicles (EVs) and for load-leveling electric grid systems,[1–6] require vast improvement in terms of power and energy densities. Typically, active materials for LIBs are either insulating or semi-conducting in nature, which seriously limits their performance. Various approaches, such as particle-size reduction,[7–10] metal ion doping,[11–14] and conductive material coating,[6,15–17] have been employed to increase the electronic conductivity of these materials. Also, conductive additives such as carbon black and carbon nanotubes have been physically mixed with the active material to enhance its electronic conductivity. Such conductive additives do not directly contribute to the battery performance and increase the total weight of the electrode.

Recently, graphene has been reported to be a suitable conductive substrate to grow active materials for energy storage applications due to its superior electrical conductivity, high mechanical strength, chemical stability, high surface-to-volume ratio, light weight and structural flexibility.[18–20] In previous studies of graphene hybrid electrodes, various metal oxides such as SnO_2,[21–23] Mn_3O_4,[24] MoO_2,[25,26] TiO_2,[27,28] and Fe_3O_4[29–31] have been grown on graphene sheets. However, growth of complex structures and compositions on a graphene surface such as the growth of $LiMn_{1-x}Fe_xPO_4$ (LMFP)[32,33] nanorods and $Li_3V_2(PO_4)_3$ (LVP)[34,35] particles on graphene are rarely reported due to the difficulties in processing. In addition, they require further addition of conductive carbon during electrode fabrication to establish the conductive network, thus under-utilizing the superior properties of graphene. This shows that active material-loaded graphene sheets in these hybrids are not interconnected and remain electrically isolated. Ideally, graphene with its two-dimensional structure (high aspect ratio) and good inherent conductivity should exhibit a low percolation threshold as reported in polymeric nanocomposites and hybrid

[a]*Department of Materials Science and Engineering, Korea Advanced Institute of Science and Engineering (KAIST), 335 Gwahangno, Yuseong-gu, Daejeon, 305-701, Republic of Korea. E-mail: dkkim@kaist.ac.kr; Fax: +82 42 350 3310; Tel: +82 42 350 4118*

[b]*Department of Materials Science and Engineering, Stanford University, 476 Lomita Mall, McCullough 343, Stanford, California 94305, USA*

† Electronic supplementary information (ESI) available: Additional rate capability data and the equipment circuit along with the fitted results of EIS data. See DOI: 10.1039/c3ta10254h

materials,[36,37] where a small weight fraction of graphene is sufficient to establish the conductive network, *i.e.* graphene-based hybrids ideally do not require any additional conductive carbon for electrode fabrication. This demonstrates that even though an individual graphene nanosheet is highly conductive, integration of it to form highly inter-connected multifunctional structures plays a critical role in energy storage devices.

Herein, a two-step approach is developed to grow a multi-component active material such as $LiTi_2(PO_4)_3$ (LTP) on a reduced graphene oxide (rGO) surface and an electrode with only 1.79% of rGO (no additional carbon added during electrode fabrication) is shown to exhibit high electrical conductivity, high rate capability (capacity retention of ~92% at 1 C compared to 0.1 C), and cycling stability (capacity retention of ~92% at 10 C after 100 cycles) as a cathode in a lithium ion battery. LTP is chosen as a model system due to the fact that LTP with a NASICON structure has a three-dimensional open framework, which allows faster ionic diffusion within various lattice sites.[38,39] This eliminates the rate capability limitation by a lithium ion diffusion process, thereby allowing the study of the effect of graphene nanosheets on electronic conductivity and therefore the power capability of the electrode.

We demonstrate that such high temperature formation of active materials on graphene oxide (GO) and simultaneous reduction of GO could result in a compact, well-connected graphene network requiring no additional conductive carbon to facilitate fast electron transport to the current collector. Such an electrode with ultralow conductive carbon would allow higher active material loading and higher specific energy density. The advantage of high temperature treatment is not just limited to the highly inter-connected graphene network, but it also helps to achieve sp^2 hybridized carbon structures.[40–42] Here, graphene not only acts as a stable, conductive substrate but also helps to control the size of the formed particles. Also, the random orientation of rGO nanosheets in the hybrid helps to create voids, resulting in a porous electrode structure, enabling efficient infiltration of electrolyte to the active material surface.

2 Experimental

Preparation of graphene oxide

Graphite oxide (GO) was synthesized from graphite powder (SP-1, 30 μm nominal particle size, Bay Carbon, Bay City, MI) by a modified Hummers method, in which pre-oxidation of graphite was carried out as reported by Kovtyukhova *et al.*[43] and followed by oxidation using the Hummers method.[44]

Synthesis of rGO–LTP hybrids

In a typical synthesis, ~40 mg of GO was added to 50 ml of DDI water and the solution was then poured into 700 ml of ethanol and heated to 80 °C under vigorous stirring. Another 50 ml of ethanol consisting of 0.75 ml of H_2SO_4 and 1.8 ml of $Ti(O(CH_2)_3CH_3)_4$ was mixed with the diluted GO solution. The mixture was continuously and vigorously stirred for more than 12 h. The formed GO–TiO_2 hybrid was centrifuged and washed with DDI water for few times. After centrifugation, the GO–TiO_2 hybrid was redispersed into 100 ml of DDI water and 0.177 g of GO–TiO_2, 0.1459 g of $LiCOOCH_3$, 0.4935 g of $(NH)_4H_2PO_4$ and 0.02 g of sucrose were mixed together in DDI water. The mixture was dried at 80 °C and the solid was heated at 900 °C for 12 h at a rate of 5 °C min^{-1} under argon gas flow in a tube furnace.

Coin cell fabrication and electrochemical measurements

Coin-type cells (CR2032) were assembled in an argon filled glove box and a polypropylene membrane (Celgard Inc.) was used as the separator. The cells consisted of 92 wt% rGO–LTP and 8 wt% of polyvinylidene fluoride (PVDF). A 1 M $LiPF_6$ dissolved in a 1 : 1 v/v mixture of ethylene carbonate (EC) and dimethyl carbonate (DMC) was used as the electrolyte. The electrochemical performance of the rGO–LTP was then measured at room temperature using a WonATech WBCS3000 and a Biologic VMP3 multichannel system. The rGO–LTP loading was 0.7–1.0 mg cm^{-2} with an electrode thickness of ~10 μm and the energy and power densities were calculated based on the rGO–LTP hybrid weight.

Characterization

Scanning electron microscopy (SEM) was carried out on an UHR-SEM Magellan 400 to examine the morphology of the hybrid material. The microstructure of rGO–LTP was observed using a Cs-Corrected Scanning Transmission Electron Microscope (STEM; JEOL). The crystal structure was confirmed by XRD (Rigaku, D/MAX-RB diffractometer, Tokyo, Japan) using Cu Kα and the patterns were collected at 0.01 step widths in the angle between 10° and 50° reflection. Elemental analysis was carried out using a Thermo Scientific Flash 2000. The quality of graphene was measured using X-ray Photoelectron spectroscopy (XPS, Sigma Probe). The quality of graphene was analyzed by Raman spectroscopy (LabRAM).

3 Results and discussion

The fabrication of rGO–LTP hybrids *via* a two-step approach is schematically illustrated in Fig. 1. Scanning electron microscopy (SEM) images in Fig. 1a show the smooth surface of the as-prepared graphene oxide (GO), where GO was prepared using a modified Hummers method.[43,44] In the first step, amorphous anatase TiO_2 nanoparticles were selectively grown on GO nanosheets suspended in ethanol by a controlled hydrolysis of titanium butoxide at 80 °C for 12 h. Adjustment of both the ratio of water/ethanol and sulfuric acid is as important as the reaction temperature to control the hydrolysis rate of titanium alkoxide, which affects the uniform formation of TiO_2 nanoparticles. Both SEM (Fig. 1b) and transmission electron microscopy (TEM) (Fig. 2a) images show the uniform growth of TiO_2 nanoparticles of approximately 5 nm on the GO surface. Furthermore, there are no free TiO_2 nanoparticles observed in the SEM images (Fig. 1b), which indicates that the free TiO_2 nanoparticles have been washed out thoroughly during the washing process. The X-ray diffraction (XRD) pattern (Fig. 2b) of the formed GO–TiO_2 hybrid is indexed to the anatase phase, which corresponds to JCPDS data no. 22-1272.

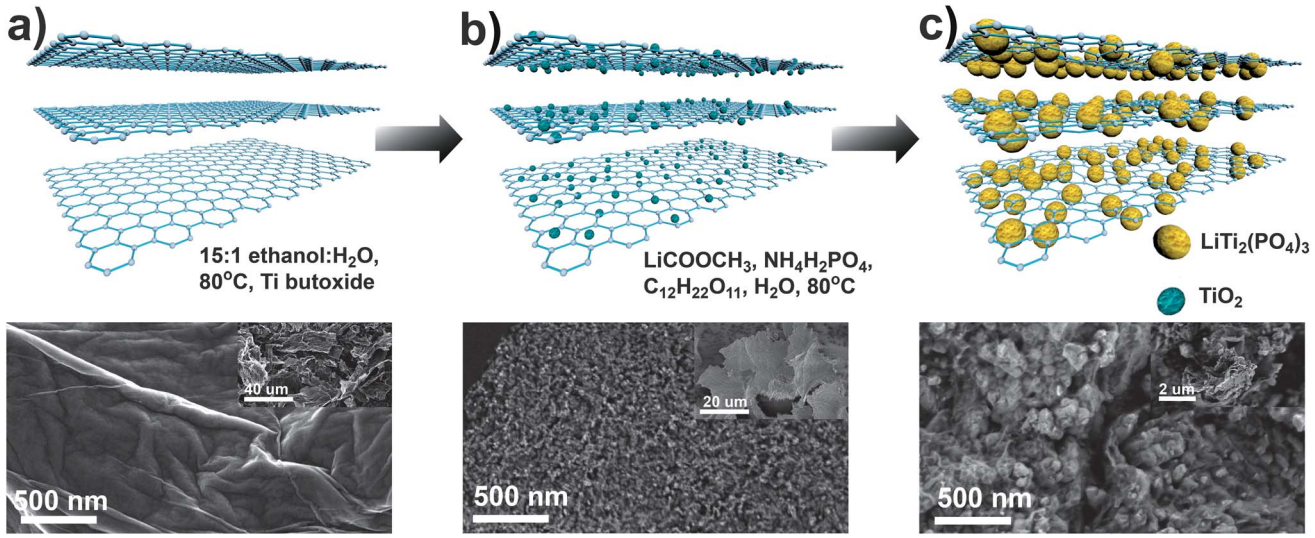

Fig. 1 Schematic of the synthesis steps (top) involved in the growth of LTP particles on an rGO surface and their corresponding SEM images (bottom). (a) GO, (b) TiO_2 precursor nanoparticles on GO and (c) LTP particles grown on the rGO surface after the second step of the solid state reaction at 900 °C for 12 h. The insets show the corresponding low magnification SEM images. These SEM images clearly show the growth of LTP particles on both sides of graphene.

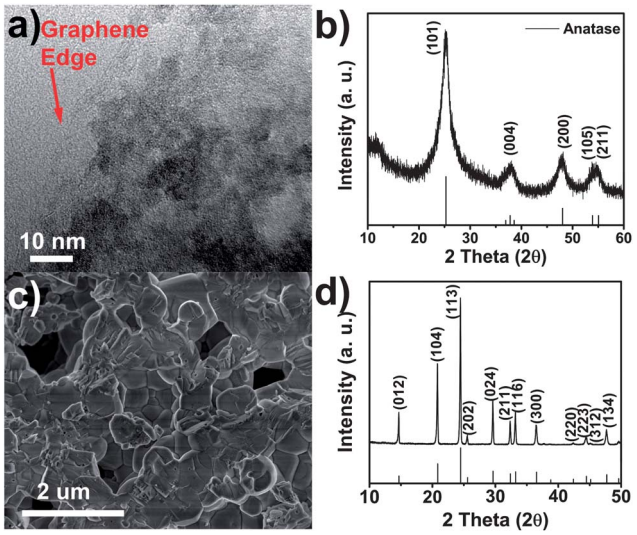

Fig. 2 Representative (a) HRTEM image of precursor TiO_2 nanoparticles grown on GO and (b) the XRD spectrum of the GO–TiO_2 hybrid. This image and the XRD spectrum confirm the growth of anatase TiO_2 nanoparticles on the GO surface. The size of the TiO_2 nanoparticles is approximately 5 nm. (c) Representative SEM image and (d) the XRD spectrum of the as-synthesized LTP control sample prepared using similar conditions to the rGO–LTP hybrid but without the addition of rGO. The SEM image shows a larger particle size with highly agglomerated structures.

In the second step, the formed oxide–GO precursor was mixed with a stoichiometric ratio of lithium acetate and ammonium dihydrogen phosphate in an aqueous medium and the mixture was allowed to dry at 80 °C under an ambient atmosphere. The dried precursor was allowed to undergo a solid state reaction at 900 °C for 12 h under an argon atmosphere to form LTP on the graphene surface (rGO–LTP) and simultaneously reduce the GO (as discussed in the later section). The low melting temperature of both precipitated lithium and phosphate sources[45] on TiO_2 nanoparticles (Fig. S1 in ESI† shows no growth of TiO_2 nanoparticles when GO–TiO_2 hybrids were heat-treated at 900 °C under an Ar atmosphere without the addition of Li and PO_4 precursors, and the particle size was still maintained below 10 nm) has induced a diffusion and dissolution–precipitation mechanism during the formation of LTP on graphene and enabled an intimate attachment between LTP particles and the basal plane of graphene. The resulting Ostwald ripening leads to the growth of LTP particles of a sub-micrometer scale. The formed LTP particles are well dispersed and anchored on the surface of rGO with a particle size of around 200 nm (Fig. 1c), which could be bonded to rGO through Ti/P–O–C bonds at the remaining oxygen sites and by van der Waals interactions with the aromatic region of rGO as reported in other phosphate–graphene hybrid materials.[32] Wrinkled morphologies of graphene are observed even after the growth of LTP *via* the solid-state reaction. These wrinkles are generated due to the thermodynamic instability of graphene to create an intrinsically stable interior. The resulting rGO hybrid is highly compact and well-interconnected, providing a good conductive pathway. In contrast, a control sample of bare LTP prepared using the same procedure without the addition of GO resulted in larger particles with a highly aggregated structure (Fig. 2c). The XRD pattern (Fig. 2d) of bare LTP can be indexed to a rhombohedral phase with a space group of *R*3*c*, which corresponds to JCPDS data no. 35-0754. To elucidate the structure of the prepared rGO–LTP hybrid, scanning transmission electron microscopy (STEM) was carried out and the dark field and the bright field images are shown in Fig. 3a and b, respectively. These images reveal that sub-micrometer sized LTP particles have grown on the graphene surface, which is more evident in the dark field image. High resolution transmission electron microscopy (HRTEM) image (Fig. 3c) shows the crystal lattice fringes in the marked white rectangular area in Fig. 3b. Their inter-planar *d*-spacing of 5.997 Å agrees well with the *hkl* of (012) of the LTP. The inset of

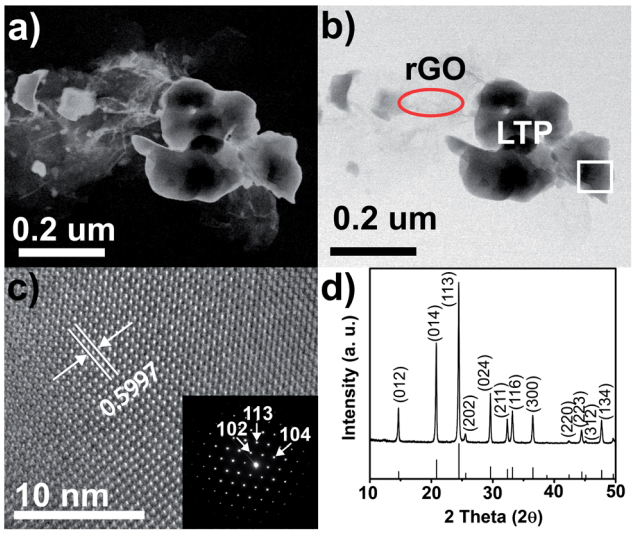

Fig. 3 (a) Dark field, (b) bright field TEM images of the rGO–LTP sample, (c) the HRTEM image of the boxed area in (b) and the inset showing the SAED pattern of the lattice structure in (c) and (d) the representative XRD pattern of rGO–LTP.

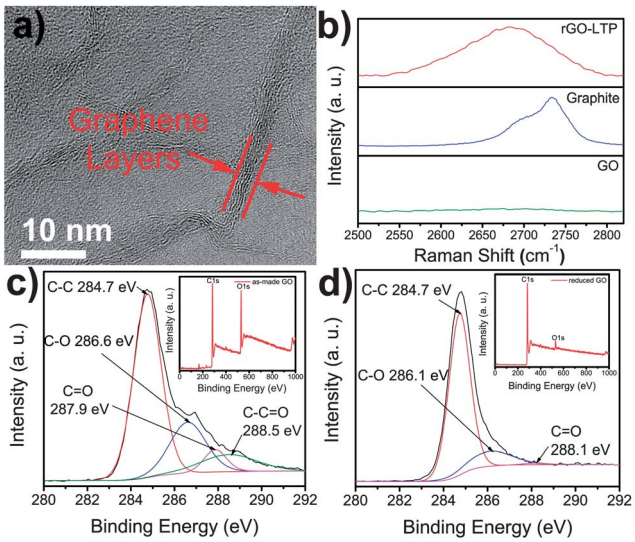

Fig. 4 (a) HRTEM image of graphene folding marked by a red circle in Fig. 3(b). (b) Raman spectra of the 2D peak of as-made GO, graphite, and rGO–LTP. The 2D peak of the rGO–LTP sample at around 2700 cm^{-1} is shifted to the left compared to the graphite sample and is very broad, which indicates the presence of a mixture of single and few-layer graphene sheets. High resolution XPS spectra of deconvoluted C 1s spectra of (c) as-made GO (inset: XPS survey of GO) and (d) of rGO (inset: XPS survey of rGO), which was thermally reduced at 900 °C from GO under the same conditions as those used to synthesize LTP particles on rGO. The drastic increase in the C/O ratio of rGO (~8.8) in comparison with as-made GO (~1.4) indicates substantial reduction of GO.

Fig. 3c, which shows the corresponding selected area electron diffraction (SAED) pattern from the LTP particle, reveals that the LTP particles on rGO are single crystalline in nature. The SAED pattern and the XRD pattern in Fig. 3d are indexed to the NASICON phase with high crystallinity, although it was synthesized at a relatively lower temperature and in a shorter time period than other reported results.[15,46]

The number of layers of graphene as well as its quality is known to strongly influence its intrinsic properties. Therefore, the quality and the number of layers of the resulting rGO in the hybrid were characterized using HRTEM, Raman and X-ray photoelectron spectroscopic (XPS) techniques. From an rGO folded area (indicated by a red circle in Fig. 3b), we can observe that less than 10 layers of graphene (Fig. 4a) are attained owing to the presence of LTP particles on the rGO surface, which prevent it from further restacking during thermal treatment. In addition, Raman spectra (Fig. 4b) show the presence of a 2D band at 2700 cm^{-1}, which is the characteristic band of graphene to determine the number of layers, indicating the predominant presence of less than 5 layers of graphene in the sample to enable a 2D peak to be detected.[47–49] Also, the two broad peaks present around 1365 cm^{-1} and 1605 cm^{-1} are assigned to the D and G bands, respectively. Further, the elemental analysis of the rGO–LTP sample indicated a total carbon content of only 1.79%. Such a small amount of graphene is enough to anchor all LTP particles due to the fact that graphene nanosheets have a very high surface area, indirectly indicating that the rGO nanosheets remain unstacked even after the solid state reaction at 900 °C. Moreover, there is no corresponding graphite peak in the XRD pattern (Fig. 3d) due to the stacking of graphene layers, which indicates that the current synthetic strategy can prevent aggregation of graphene layers during the formation of hybrid materials at high temperature.

XPS was employed to characterize the thermally reduced GO to analyze its chemical composition. As shown in Fig. 4c, the absorbance peak of the C1s XPS spectrum of GO has three components of oxygen functionalities at 286.6 eV (C–O), 287.9 eV (C=O), and 288.5 eV (C–C=O).[50–52] The detected oxygen functionalities indicate a considerable degree of oxidation in the as-prepared GO. Although the C1s XPS spectrum of rGO in Fig. 4d still retains some oxygen functionalities even after thermal treatment at 900 °C, the peak areas and intensities have decreased drastically and are negligible compared to the GO spectrum. In addition, it is impossible to deconvolute the carboxylate (C–C=O) peak at 288.5 eV due to its negligible amount when GO is heated above 800 °C as reported in the literature.[53] At the same time, the sp^2 (C–C) hybridized carbon is also increased from ~54% to ~83% after thermal reduction, which indicates considerable deoxygenation during thermal treatment. Also, the XPS survey spectra shown in the insets of Fig. 4c and d reveal that the C/O ratio drastically increased from ~1.4 to ~8.8 upon thermal reduction, indirectly indicating the enhancement in the electronic conductivity with a significant removal of oxygen.[51] Consequently, the superior characteristics of graphene such as electrical and thermal conductivity are well-retained with less deterioration.

Coin cells were assembled to characterize the electrochemical performance of the rGO–LTP hybrid as the cathode (consisting of 92 wt% rGO–LTP and 8 wt% PVDF binder) and Li foil as the anode. All the cells were cycled between 1.5 and 3.5 V under constant current at the same charge–discharge rates for each C rate based on the theoretical specific capacity of LTP, where 1 C rate corresponds to a current density of 138 mA g^{-1}. A typical charge–discharge curve of the rGO–LTP hybrid electrode

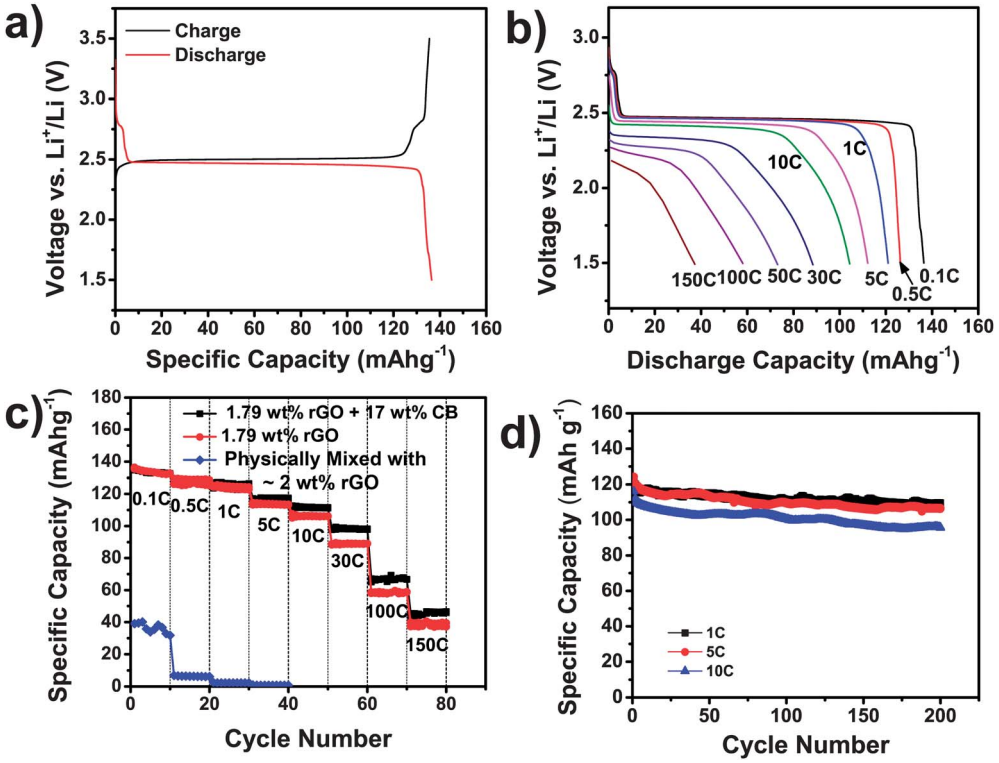

Fig. 5 Electrochemical characterizations of the rGO–LTP hybrid as a cathode material in the lithium battery; (a) representative charge and discharge curves at a rate of C/10, (b) discharge curves at various C rates, (c) specific discharge capacities at various incremental C rates (the discharge cut-off voltage was 1.5 V *vs.* Li^+/Li and 10 cycles for each C rate), and (d) long term cycling performance at the charge–discharge rates of 1, 5, and 10 C.

at a rate of C/10 (Fig. 5a) displays a voltage plateau at 2.48 V. The electrode delivered a discharge capacity of 134 mA h g^{-1} and 136 mA h g^{-1} by considering the mass of the active material and the hybrid, respectively, which are close to the theoretical capacity. Fig. 5b presents the discharge curves of the rGO–LTP hybrid at various discharge rates between C/10 and 150 C, using a charge rate that is the same as the discharge rate. The specific capacity of 123 mA h g^{-1} was obtained at a discharge rate of 1 C, which is ~92% of the theoretical specific capacity based on the weight of the active material. The discharge capacity of the rGO–LTP sample decreased to 116, 110, 103, and 83 mA h g^{-1} when the rate was increased to 5, 10, 20, and 50 C, respectively. Further increases in the discharge rate to 100 C and 150 C (corresponding to a discharge time of 36 s and 24 s, respectively) delivered specific capacities of 58 and 37 mA h g^{-1}, respectively. In addition, the discharge curves of rGO–LTP show its capability to retain the flat plateau around 2.45 V even at a high charge–discharge rate of 50 C, indicating that the discharge reaction still proceeds *via* a first order phase transition between LTP and $Li_3Ti_2(PO_4)_3$. Also, the electrode overpotential was almost negligible even at a very high rate of 10 C. The growth of LTP on highly conductive graphene has facilitated fast electron transport due to a strong electrical coupling between LTP and graphene and renders a high specific capacity even at high charge–discharge rates. Also, few-layer graphene exhibits a large specific surface area (2000 m^2 g^{-1}) and the voids between the graphene layers facilitate the easy access of electrolyte to the surface active materials. Furthermore, the control of particle size to the sub-micrometer range using graphene has rendered a shorter lithium ion diffusion path length. These factors lead to high discharge capacities, and enable a flat plateau to be maintained even at high current densities.

Also, cells were fabricated with the electrode containing additional carbon (electrode composition – 75 wt% rGO–LTP, 17 wt% carbon black (CB), and 8 wt% PVDF) as a control sample. Generally, the addition of 17 wt% CB could assist in enhancing the rate capability as CB covers the exposed surface area of LTP particles on rGO and form an interconnected network to deliver electrons to rGO at a high current density.[54] Remarkably, both the cells exhibit similar electrochemical behavior such as specific capacity and rate capability (Fig. 5c). Additionally, both electrodes demonstrate highly reversible behavior as shown in ESI, Fig. S2a.† Another data set (ESI, Fig. S2b†) from a different batch of rGO–LTP confirmed the repeatability of rGO–LTP. These results signify that the strong electrical coupling between rGO and LTP[55] through chemical bonding along with the formation of a highly inter-connected rGO network has led to fast electron transportation from the active materials to the current collector, thereby eliminating the need for additional carbon black in the electrode.

To confirm these advantages, bare LTP particles were physically mixed with ~2 wt% of rGO and their electrochemical performance was studied. At a low charge–discharge rate of 0.1 C, the rGO mixed LTP sample delivered a discharge capacity of ~40 mA h g^{-1} which was only 30% of the theoretical capacity (138 mA h g^{-1}). A negligible discharge capacity was obtained at

the higher charge–discharge rates of 5 C (Fig. 5c). In contrast, rGO–LTP hybrid materials with the same amount of conductive graphene could maintain their discharge capacity of ~40 mA h g^{-1} even at a charge–discharge rate as high as 150 C. Apart from the rate capability, cycling tests were also conducted to evaluate the durability of the rGO–LTP hybrid electrode at higher rates and fresh cells were used in all cycling tests. Fig. 5d shows the cycling behavior at charge–discharge rates of 1, 5, and 10 C, demonstrating the capacity retention of about ~92% of its initial specific capacity at the 1 C rate after 100 cycles. At a higher charge–discharge rate of 10 C, the specific capacity could still be maintained over 100 mA h g^{-1}after 100 cycles.

To understand the remarkable rate performance of the rGO–LTP hybrid compared to the rGO mixed LTP, electrochemical impedance spectroscopy (EIS) measurements were performed for both the samples before cycling. The kinetic charge-transfer resistance at the electrode/electrolyte interface of the rGO–LTP hybrid materials and rGO mixed LTP were analyzed based on a modified Randles equivalent circuit (ESI, Fig. S3†). As demonstrated in Fig. 6a, the Nyquist plots show that the depressed semicircle of rGO–LTP hybrids in the high-medium frequency region, in which their diameter is much smaller than that of the rGO mixed LTP, suggests that rGO–LTP possesses a lower charge-transfer resistance. The charge-transfer resistance (R_{ct} = 40.37 Ohms) of rGO–LTP hybrid materials is significantly lower than that of the rGO mixed LTP (R_{ct} = 202.60 Ohms) and *vice versa* for the exchange current density ($i_o = RT/nFR_{ct}$) as shown in ESI, Table S1.† This result indicates that the graphene in the rGO–LTP hybrid not only decreases R_{ct} and increases the conductivity of the overall electrode, but also largely enhances the electrochemical activity of LTP during cycling.

To further emphasize the significance of this method, the obtained specific capacity was calculated based on the total mass of the electrode. As one can observe from Fig. 6b, the rGO–LTP electrode fabricated without additional CB shows a remarkable improvement of over 20% capacity up to 5 C rate and 10% capacity improvement even at the 100 C rate in comparison with CB added samples. Therefore, compact lithium ion batteries with higher active material loading can be developed using such a CB-free electrode fabrication approach.

Fig. 6c shows the comparison of Ragone plots of rGO–LTP samples fabricated with and without adding CB with other phosphate based materials reported in the literature. The calculated power and energy densities are normalized based on the mass of the active materials, enabling comparison with the literature values of LFP and LMP samples,[45] which contain a higher total carbon content. Although, the rGO–LTP sample shows a slightly lower specific energy due to its low voltage plateau, the Ragone plot comparison indicates that the specific power of LTP is much higher than that of both the LFP and LMP samples. Typically, LFP and LMP require a galvanostatic–potentiostatic mode of charging to increase their capacity, whereas only the galvanostatic mode was used for charging in the current work. Charging and discharging were done at the same rate. The rGO–LTP hybrid is still capable of maintaining the specific energy around 210 W h kg^{-1} with no obvious decrease even at a very high specific power up to 10 000 W kg^{-1}. This signifies that the cell fabricated with just 1.79% of conductive carbon can be charged and discharged in 36 s while maintaining the specific energy density above 200 W h kg^{-1}. This is one of the best reported results so far for highly insulating phosphate based hybrid materials. Furthermore, the amount of conductive carbon used in the rGO–LTP hybrid electrodes is as low as 1.79 wt% in total mass, which is much lower than in other reported results.

In order to understand the high durability achieved by rGO–LTP (with carbon black) at higher rates, its structural change during cycling was scrutinized using *ex situ* HRTEM and XRD studies (Fig. 7). The cells were cycled at a rate of 5 C for 200 cycles prior to structural characterization. There is no noticeable lattice change after 200 cycles in a charged state in the HRTEM image (Fig. 7a and b). Its corresponding SAED pattern is also identical with the LTP phase, which indicates its capability to return to the initial state even after long cycles at a high rate. To further investigate the effect of cycling on structural changes, *ex situ* XRD (Fig. 7c) was carried out after the first cycle and the 200th cycle at charged states and its corresponding charge–discharge curves are shown in Fig. 7d (ESI, Fig. S4† shows the cycling behavior of the rGO–LTP sample with and without carbon black at 5 C charge–discharge rate for 200

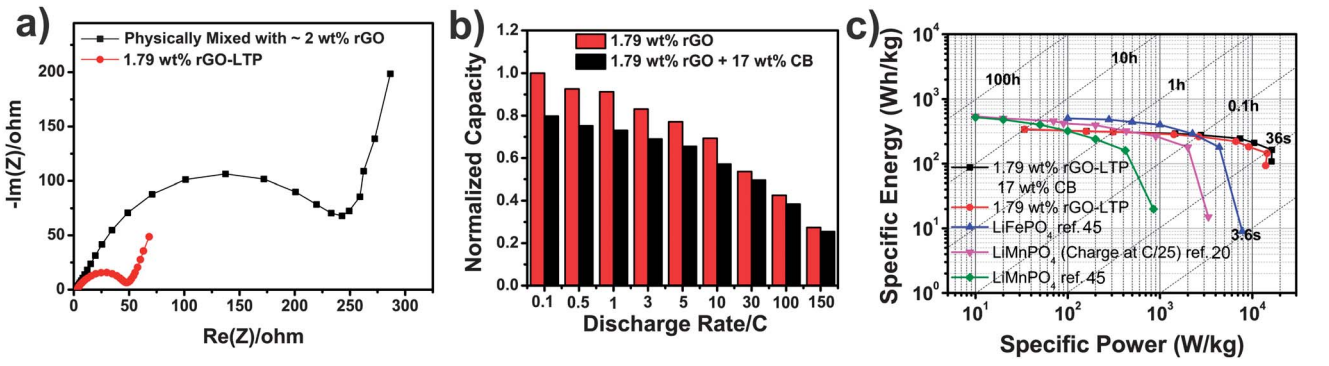

Fig. 6 (a) Electrochemical impedance spectra of the rGO–LTP hybrid electrode fabricated without the addition of CB and a physically mixed LTP and rGO sample. (b) Specific capacities based on the total mass of the electrode fabricated with and without CB at various C rates, and (c) comparison of Ragone plots of the rGO–LTP sample fabricated with and without CB with other phosphate based cathode materials reported in the literature.

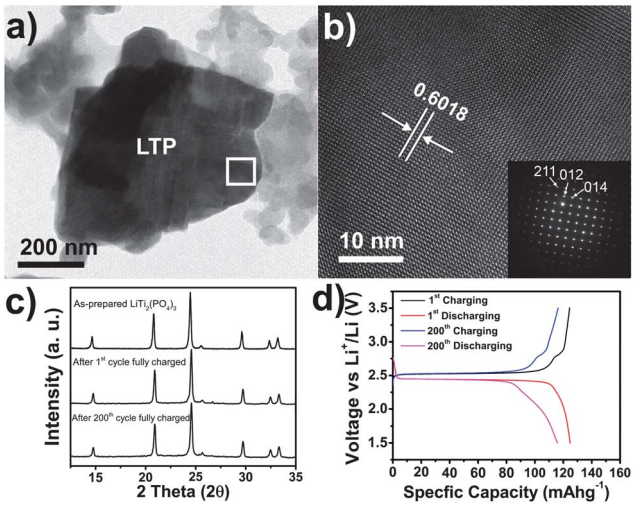

Fig. 7 Physical and electrochemical characterization of rGO–LTP after 200 charge–discharge cycles at a 5 C rate. (a) Representative TEM image of rGO–LTP after charging to 3.5 V. (b) High-resolution TEM image of the LTP particles on rGO (boxed area in (a)). Inset: selected area diffraction (SAED) pattern of the lattice structure in (b). (c) *Ex situ* XRD spectra of rGO–LTP at 1st and 200th charged states. For comparison, the documented XRD spectra of as-prepared LTP are plotted together and (d) 1st and 200th charge and discharge curves of rGO–LTP at a rate of 5 C.

cycles). The *ex situ* results show that the XRD profiles of the 1st cycle and the 200th cycle charged state do not have significant changes indicating topotactic Li insertion into a rhombohedral structure and maintaining zero-strain characteristics. The observed stability of rGO–LTP in galvanostatic cycling signifies the importance of rGO as a volume buffer during intercalation (expansion) and extraction (contraction) to prevent the fracture of LTP.

The successful bridging of LTP particles with graphene nanosheets as a conductive network has significantly improved the electrochemical performance of the hybrid material, since this intimate interaction has facilitated an effective and rapid charge carrier transport back and forth between the rGO–LTP and current collector *via* graphene networking. Good interaction of LTP with graphene also yields good dispersion of LTP particles on graphene and avoids aggregation upon cycling, which are traits that aid cycling stability. Furthermore, graphene has hindered the agglomeration of particles during solid-state reaction and hence reduce the lithium ion diffusion path length as the particle size is smaller than bare LTP, favouring a high-rate performance. Therefore, the rGO–LTP hybrid materials have improved electronic and ionic conductivities, which result in excellent enhancement in specific capacity, rate capability, higher reversibility as well as stable cycleability.

4 Conclusions

In summary, we have demonstrated that the facile growth of LTP particles on a graphene surface at high temperature forms a highly conductive well inter-connected rGO–LTP hybrid. Its utilization for Li-ion batteries with a total carbon content of only 1.79 wt% exhibits superior specific capacity, excellent cycling, and rate capability. In addition, the rGO nanosheets perform the multiple roles of controlling the particle size during synthesis and rendering stability during cycling. Overall, the rGO–LTP electrode with no additional carbon shows better electrochemical performance and energy density than the rGO–LTP electrode with additional carbon black. We believe that this simple and low cost strategy will provide a new pathway to overcome the challenges of growing multi-component systems on highly inter-connected graphene nanosheets without any particle agglomeration on a large-scale for energy storage and other advanced applications.

Acknowledgements

This work was supported by the Program to Solve Climate Changes (NRF-2010-C1AAA001-2010-0029031), the Priority Research Centers Program (2011-0031407), and the Pioneer Research Center Program (2010-0019469) through the National Research Foundation of Korea (NRF) funded by the Ministry of Education, Science and Technology. H. W. Lee was financially supported by the Basic Science Research Program through the National Research Foundation of Korea (NRF) funded by the Ministry of Education, Science and Technology (2012038593).

Notes and references

1 Y. J. Lee, H. Yi, W.-J. Kim, K. Kang, D. S. Yun, M. S. Strano, G. Ceder and A. M. Belcher, *Science*, 2009, **324**, 1051–1055.
2 C. D. Wessells, S. V. Peddada, R. A. Huggins and Y. Cui, *Nano Lett.*, 2011, **11**, 5421–5425.
3 B. Dunn, H. Kamath and J.-M. Tarascon, *Science*, 2011, **334**, 928–935.
4 M. Armand and J. M. Tarascon, *Nature*, 2008, **451**, 652–657.
5 X. Ji, K. T. Lee and L. F. Nazar, *Nat. Mater.*, 2009, **8**, 500–506.
6 X.-L. Wu, L.-Y. Jiang, F.-F. Cao, Y.-G. Guo and L.-J. Wan, *Adv. Mater.*, 2009, **21**, 2710–2714.
7 C. Wessells, F. La Mantia, H. Deshazer, R. A. Huggins and Y. Cui, *J. Electrochem. Soc.*, 2011, **158**, A352–A355.
8 H.-W. Lee, P. Muralidharan, R. Ruffo, C. M. Mari, Y. Cui and D. K. Kim, *Nano Lett.*, 2010, **10**, 3852–3856.
9 P. Gibot, M. Casas-Cabanas, L. Laffont, S. Levasseur, P. Carlach, S. Hamelet, J. M. Tarascon and C. Masquelier, *Nat. Mater.*, 2008, **7**, 741–747.
10 M. K. Devaraju and I. Honma, *Adv. Energy Mater.*, 2012, **2**, 284–297.
11 D. Capsoni, M. Bini, S. Ferrari, P. Mustarelli, V. Massarotti, M. C. Mozzati and A. Spinella, *J. Phys. Chem. C*, 2010, **114**, 13872–13878.
12 H. Peng, H. Xie and J. B. Goodenough, *J. Power Sources*, 2012, **197**, 310–313.
13 S.-Y. Chung, J. T. Bloking and Y.-M. Chiang, *Nat. Mater.*, 2002, **1**, 123–128.
14 H. Li, Z. Wang, L. Chen and X. Huang, *Adv. Mater.*, 2009, **21**, 4593–4607.
15 J.-Y. Luo and Y.-Y. Xia, *Adv. Funct. Mater.*, 2007, **17**, 3877–3884.
16 J.-Y. Luo and Y.-Y. Xia, *J. Power Sources*, 2009, **186**, 224–227.

17 C. Zhu, Y. Yu, L. Gu, K. Weichert and J. Maier, *Angew. Chem., Int. Ed.*, 2011, **50**, 6278–6282.
18 A. K. Geim and K. S. Novoselov, *Nat. Mater.*, 2007, **6**, 183–191.
19 S. Park and R. S. Ruoff, *Nat. Nanotechnol.*, 2009, **4**, 217–224.
20 C.-J. Shih, A. Vijayaraghavan, R. Krishnan, R. Sharma, J.-H. Han, M.-H. Ham, Z. Jin, S. Lin, G. L. C. Paulus, N. F. Reuel, Q. H. Wang, D. Blankschtein and M. S. Strano, *Nat. Nanotechnol.*, 2011, **6**, 439–445.
21 X. Zhou, Y.-X. Yin, L.-J. Wan and Y.-G. Guo, *J. Mater. Chem.*, 2012, **22**, 17456–17459.
22 C.-M. Chen, Q. Zhang, J.-Q. Huang, W. Zhang, X.-C. Zhao, C.-H. Huang, F. Wei, Y.-G. Yang, M.-Z. Wang and D. S. Su, *J. Mater. Chem.*, 2012, **22**, 13947–13955.
23 T. Chen, L. Pan, X. Liu, K. Yu and Z. Sun, *RSC Adv.*, 2012, **2**, 11719–11724.
24 H. Wang, L.-F. Cui, Y. Yang, H. Sanchez Casalongue, J. T. Robinson, Y. Liang, Y. Cui and H. Dai, *J. Am. Chem. Soc.*, 2010, **132**, 13978–13980.
25 K. H. Seng, G. D. Du, L. Li, Z. X. Chen, H. K. Liu and Z. P. Guo, *J. Mater. Chem.*, 2012, **22**, 16072–16077.
26 F. Xia, X. Hu, Y. Sun, W. Luo and Y. Huang, *Nanoscale*, 2012, **4**, 4707–4711.
27 Y. Liang, H. Wang, H. Sanchez Casalongue, Z. Chen and H. Dai, *Nano Res.*, 2010, **3**, 701–705.
28 P. Dong, Y. Wang, L. Guo, B. Liu, S. Xin, J. Zhang, Y. Shi, W. Zeng and S. Yin, *Nanoscale*, 2012, **4**, 4641–4649.
29 S. Yang, X. Feng, S. Ivanovici and K. Müllen, *Angew. Chem., Int. Ed.*, 2010, **49**, 8408–8411.
30 R. Wang, C. Xu, J. Sun, L. Gao and C. Lin, *J. Mater. Chem. A*, 2013, **1**, 1794–1800.
31 C. Wang, Q. Zhang, Q.-H. Wu, T.-W. Ng, T. Wong, J. Ren, Z. Shi, C.-S. Lee, S.-T. Lee and W. Zhang, *RSC Adv.*, 2012, **2**, 10680–10688.
32 H. Wang, Y. Yang, Y. Liang, L.-F. Cui, H. Sanchez Casalongue, Y. Li, G. Hong, Y. Cui and H. Dai, *Angew. Chem., Int. Ed.*, 2011, **50**, 7364–7368.
33 J. Zhou, J. Wang, L. Zuin, T. Regier, Y. Hu, H. Wang, Y. Liang, J. Maley, R. Sammynaiken and H. Dai, *Phys. Chem. Chem. Phys.*, 2012, **14**, 9578–9581.
34 H. Liu, P. Gao, J. Fang and G. Yang, *Chem. Commun.*, 2011, **47**, 9110–9112.
35 H. Liu, G. Yang, X. Zhang, P. Gao, L. Wang, J. Fang, J. Pinto and X. Jiang, *J. Mater. Chem.*, 2012, **22**, 11039–11047.
36 M. Yoonessi and J. R. Gaier, *ACS Nano*, 2010, **4**, 7211–7220.
37 Y. Yang, C. Wang, B. Yue, S. Gambhir, C. O. Too and G. G. Wallace, *Adv. Energy Mater.*, 2012, **2**, 266–272.
38 A. Aatiq, M. Menetrier, L. Croguennec, E. Suard and C. Delmas, *J. Mater. Chem.*, 2002, **12**, 2971–2978.
39 K. S. Nanjundaswamy, A. K. Padhi, J. B. Goodenough, S. Okada, H. Ohtsuka, H. Arai and J. Yamaki, *Solid State Ionics*, 1996, **92**, 1–10.
40 S. Pei and H.-M. Cheng, *Carbon*, 2012, **50**, 3210–3228.
41 D. Zhan, Z. Ni, W. Chen, L. Sun, Z. Luo, L. Lai, T. Yu, A. T. S. Wee and Z. Shen, *Carbon*, 2011, **49**, 1362–1366.
42 W. Gao, L. B. Alemany, L. Ci and P. M. Ajayan, *Nat. Chem.*, 2009, **1**, 403–408.
43 N. I. Kovtyukhova, P. J. Ollivier, B. R. Martin, T. E. Mallouk, S. A. Chizhik, E. V. Buzaneva and A. D. Gorchinskiy, *Chem. Mater.*, 1999, **11**, 771–778.
44 W. S. Hummers and R. E. Offeman, *J. Am. Chem. Soc.*, 1958, **80**, 1339.
45 D. Choi, D. Wang, I.-T. Bae, J. Xiao, Z. Nie, W. Wang, V. V. Viswanathan, Y. J. Lee, J.-G. Zhang, G. L. Graff, Z. Yang and J. Liu, *Nano Lett.*, 2010, **10**, 2799–2805.
46 S. Patoux and C. Masquelier, *Chem. Mater.*, 2002, **14**, 5057–5068.
47 L. M. Malard, M. A. Pimenta, G. Dresselhaus and M. S. Dresselhaus, *Phys. Rep.*, 2009, **473**, 51–87.
48 A. C. Ferrari, J. C. Meyer, V. Scardaci, C. Casiraghi, M. Lazzeri, F. Mauri, S. Piscanec, D. Jiang, K. S. Novoselov, S. Roth and A. K. Geim, *Phys. Rev. Lett.*, 2006, **97**, 187401.
49 Y. Hernandez, V. Nicolosi, M. Lotya, F. M. Blighe, Z. Sun, S. De, I. T. McGovern, B. Holland, M. Byrne, Y. K. Gun'Ko, J. J. Boland, P. Niraj, G. Duesberg, S. Krishnamurthy, R. Goodhue, J. Hutchison, V. Scardaci, A. C. Ferrari and J. N. Coleman, *Nat. Nanotechnol.*, 2008, **3**, 563–568.
50 J. Zhang, H. Yang, G. Shen, P. Cheng, J. Zhang and S. Guo, *Chem. Commun.*, 2010, **46**, 1112–1114.
51 O. C. Compton, B. Jain, D. A. Dikin, A. Abouimrane, K. Amine and S. T. Nguyen, *ACS Nano*, 2011, **5**, 4380–4391.
52 L. Tang, Y. Wang, Y. Li, H. Feng, J. Lu and J. Li, *Adv. Funct. Mater.*, 2009, **19**, 2782–2789.
53 A. Ganguly, S. Sharma, P. Papakonstantinou and J. Hamilton, *J. Phys. Chem. C*, 2011, **115**, 17009–17019.
54 K.-C. Jiang, S. Xin, J.-S. Lee, J. Kim, X.-L. Xiao and Y.-G. Guo, *Phys. Chem. Chem. Phys.*, 2012, **14**, 2934–2939.
55 H. Wang, Y. Yang, Y. Liang, J. T. Robinson, Y. Li, A. Jackson, Y. Cui and H. Dai, *Nano Lett.*, 2011, **11**, 2644–2647.

